Adiabatic transverse thermoelectric conversion enhanced by heat current manipulation in artificially tilted multilayers

Fuyuki Ando,[1,*] Takamasa Hirai,[1] Hiroto Adachi,[2] and Ken-ichi Uchida[1,3]

[1]*Research Center for Magnetic and Spintronic Materials, National Institute for Materials Science, 1-2-1 Sengen, Tsukuba, Ibaraki 305-0047, Japan*

[2]*Research Institute for Interdisciplinary Science, Okayama University, 3-1-1 Tsushimanaka, Kita-ku, Okayama, Okayama 700-8530, Japan*

[3]*Department of Advanced Materials Science, Graduate School of Frontier Sciences, The University of Tokyo, 5-1-5 Kashiwanoha, Kashiwa, Chiba 277-8561, Japan*

We phenomenologically formulate and experimentally observe an adiabatic transverse thermoelectric conversion enhanced by a heat current re-orientation in artificially tilted multilayers (ATMLs). By alternately stacking two materials with different thermal conductivities and rotating its multilayered structure with respect to a longitudinal temperature gradient, off-diagonal components in the thermal conductivity tensor are induced. This off-diagonal thermal conduction (ODTC) generates a finite transverse temperature gradient and Seebeck-effect-induced thermopower in the adiabatic condition, which is superposed on the isothermal transverse thermopower driven by the off-diagonal Seebeck effect (ODSE). In this study, we calculate and observe the two-dimensional temperature distribution and the resultant transverse thermoelectric conversion in ATMLs comprising thermoelectric Co_2MnGa Heusler alloys and $Bi_{2-a}Sb_aTe_3$ compounds. By changing the tilt angle from 0° to 90°, the transverse temperature gradient obviously appeared in the middle angles and the transverse thermopower increases up to -121.9 μV/K in $Co_2MnGa/Bi_{0.2}Sb_{1.8}Te_3$-based ATML at the tilt angle of 45° whereas the isothermal contribution is estimated to be -82.6 μV/K from the analytical calculation. This hybrid action derived from ODTC results in the significant enhancement of the maximum reduced conversion efficiency from 3.1% to 8.1% in calculation and from 2.3% to 4.4% in experiment.

I. INTRODUCTION

A transverse thermoelectric effect in solids, which mutually converts charge and heat currents in the orthogonal directions, has attracted much attention in terms of fundamental physics, materials science, and thermoelectric applications [1–4]. This unique geometry offers a practical advantage, that is, simplification of a thermoelectric device architecture only using a single material, whereas classical thermoelectric devices utilizing the Seebeck effect consist of multiple thermoelectric materials and electrodes connecting in series and forming a π-shaped structure. The most representative transverse thermoelectric effect is the Nernst effect [1]. Recently, associated with the development of spin caloritronics [4–7] and topological materials science [8–10], the studies on both the ordinary and anomalous Nernst effects have rapidly advanced and achieved the superior transverse thermoelectric performance than ever before owing to the non-trivial band topology [11–20] or extrinsic mechanisms [21–23]. Meanwhile, ODSE as the other principle has been intensively studied for wide variety of materials having microscale anisotropy, i.e., the goniopolar materials [24–28] and ($p \times n$)-type thermoelectric superlattices [29,30], and having macroscale anisotropy, i.e., ATMLs [31–35]. The ODSE materials exhibit higher performances than those by the Nernst effects. Also, the hybridization of the multiple principles in a single material also provides a key for the further advance of materials science for transverse thermoelectrics [36,37]. These recent progresses are expected to develop the next core technologies for energy harvesting and thermal management.

In addition to the insight into materials characteristics, the thermal boundary conditions, i.e., isothermal or adiabatic, also have a significant influence on the transverse thermoelectric performance [26]. The standard definition of the figure of merit for transverse thermoelectric conversion $z_{xy}T$ is given as [38–41]:

*Contact author: ANDO.Fuyuki@nims.go.jp

$$z_{xy}T = \frac{{S_{xy}}^2}{\rho_{xx}\kappa_{yy}}T. \quad (1)$$

where $S_{xy} \equiv E_x/\nabla_y T\big|_{\nabla_x T=0}$ is the isothermal transverse thermopower by the ratio of the applied temperature gradient in y-axis ($\nabla_y T$) and generated electric field in x-axis ($\mathbf{E}_x$) under the temperature gradient in x-axis $\nabla_x T = 0$ as shown in Fig. 1(a). Also, $\rho_{xx} \equiv E_x/j_{c,x}\big|_{\nabla_x T=0}$ and $\kappa_{yy} \equiv -j_{q,y}/\nabla_y T\big|_{\nabla_x T=0}$ are respectively the isothermal electrical resistivity and thermal conductivity with $j_{c,x}$ and $j_{q,y}$ being the charge current density in x-axis and heat current density in y-axis. Delves [42,43] and Horst [44,45] pointed out that when the isothermal condition of $\nabla_x T = 0$ is replaced by the adiabatic condition of $j_{q,x} = 0$, $z_{xy}T$ changes to an adiabatic figure of merit $z^*_{xy}T$ due to the appearance of finite $\nabla_x T$ and modification to the adiabatic transverse thermopower S^*_{xy}, electrical resistivity ρ^*_{xx}, and thermal conductivity κ^*_{yy}. Note that the adiabatic physical quantities are highlighted by the superscript * in this work. $\nabla_x T$ typically originates from ODTC of the applied $j_{q,y}$, such as the thermal Hall effect (i.e., Righi-Leduc effect) or anisotropy of thermal conductivity. However, the adiabatic transverse thermoelectric properties modulated by ODTC-induced $\nabla_x T$ has generally been considered for the cooling applications [12,42,44,46,47] or treated just as a correction term to explain why magneto-thermoelectric coefficients differ in the same materials, e.g., the difference in thermal boundary conditions due to the aspect ratio [19,26,43,45]. Thus, there has been no attempt to constructively utilize ODTC to improve transverse thermoelectric performance.

Materials which actively control the heat current direction have been developed to form unique thermal circuits harvesting waste heat, which are often called thermal metamaterials [48–50]. Figure 1(b) shows a schematic of ATML consisting of two materials with different thermal conductivities κ, where the effective thermal conductivities in parallel and perpendicular to the stacking plane ($\kappa_\parallel$ and $\kappa_\perp$) are different from each other. Owing to this structure-induced anisotropic thermal conductivity, the heat current bends from y-axis when $\nabla_y T$ is applied oblique to the stacking plane. Here, the off-diagonal component of the thermal conductivity tensor $\kappa_{xy} = -j_{q,x}/\nabla_y T$ in ATMLs is expressed by the analytical matrix calculation in Appendix A with Refs. [51–53] as

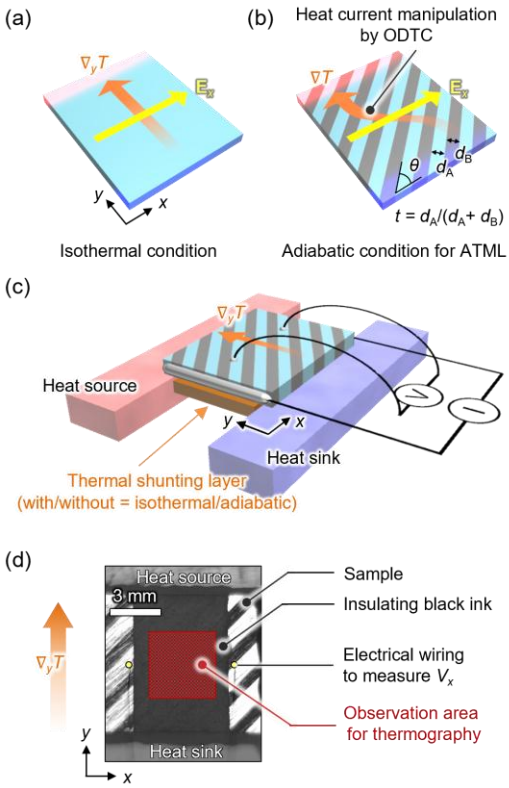

FIG 1. Schematic of transverse thermoelectric conversion in (a) isothermal condition and (b) adiabatic condition for an anisotropic material, such as ATML. By rotating the multilayer by θ to the x-axis, ODTC is induced so that the bent heat current direction modulates $\mathbf{E}_x$. (c) Schematic and (d) infrared image of the measurement configuration for the two-dimensional temperature distribution and transverse thermoelectric conversion in CMG/BT-based ATML.

$$\kappa_{xy} = (\kappa_\parallel - \kappa_\perp)\sin\theta\cos\theta, \quad (2)$$

where θ denotes the tilt angle of the stacking plane to x-axis. The $(\kappa_\parallel - \kappa_\perp)$ term increases as the difference in κ between the constituent materials increases. Then, the thermally adiabatic limit and open circuit condition [$j_{q,x} = j_{c,x} = 0$ in Eq. (A1)] gives a relationship between κ_{xy} and $\nabla_x T$ as follows:

$$\nabla_x T = -\frac{\kappa_{xy}}{\kappa_{xx}}\nabla_y T. \quad (3)$$

The previous studies experimentally observed sizable bending angles up to 26° in copper/stainless use steel-

*Contact author: ANDO.Fuyuki@nims.go.jp

based ATMLs, which corresponds to $\nabla_x T/\nabla_y T \sim -0.5$ owing to the large $-\kappa_{xy}/\kappa_{xx}$ [48,52]. Thus, there is abundant room for utilizing the bending heat current for transverse thermoelectrics by hybridizing transverse and longitudinal thermoelectric effects driven by $\nabla_y T$ and $\nabla_x T$.

In this study, we phenomenologically formulate and experimentally demonstrate the enhancement of S_{xy}^* and transverse thermoelectric conversion efficiency by combining ODSE induced by $\nabla_y T$ and the Seebeck effect induced by $\nabla_x T$ in ATMLs. We synthesized the ATML slabs comprising thermoelectric Co_2MnGa Heusler alloys and $Bi_{2-a}Sb_aTe_3$ compounds with various θ from 0° to 90°. Through the observation of two-dimensional temperature distribution using an infrared camera while applying $\nabla_y T$, the θ dependence of ODTC-induced $\nabla_x T/\nabla_y T$ was characterized and confirmed the consistency with the analytically calculated $-\kappa_{xy}/\kappa_{xx}$. As the result of the heat current re-orientation, the higher transverse thermopower of -121.9 μV/K than S_{xy} of -82.6 μV/K obtained by the conventional matrix calculation was observed in $Co_2MnGa/Bi_{0.2}Sb_{1.8}Te_3$-based ATML. Owing to the ODTC-induced enhancement of transverse thermopower, the analytically calculated $z_{xy}^* T$ reaches 0.28 in maximum at room temperature whereas the maximum $z_{xy}T$ is calculated to be 0.13, which corresponds to the 165% improvement for the transverse thermoelectric conversion efficiency. We experimentally observed the enhancement of conversion efficiency from 2.3% in the isothermal configuration to 4.4% in the adiabatic one using the same $Co_2MnGa/Bi_{0.2}Sb_{1.8}Te_3$-based ATML sample. Thus, the heat current manipulation in the adiabatic condition provides a distinct strategy on the material developments and device designs for transverse thermoelectrics.

II. METHODS

To obtain a superior ODSE-induced transverse thermopower, Co_2MnGa (CMG), $Bi_{0.2}Sb_{1.8}Te_3$ (BST), and Bi_2Te_3 (BT) were selected as the constituent materials for ATMLs. The synthesis processes and measurement methods for thermoelectric transport properties for each sintered body are detailly described in Ref. [37]. Table I shows the summary of the measurement results: the Seebeck coefficient S_{SE}, electrical resistivity ρ, and thermal conductivity κ for CMG, BST, and BT. It is found that the transport properties, especially κ, are greatly different between CMG and BST (BT), which is favorable to obtain both large ODSE and ODTC in ATMLs.

TABLE I. Thermoelectric transport properties for CMG, BST, and BT from Ref. [37].

	CMG	BST	BT
S_{SE} ($\times 10^{-6}$ V/K)	-32.1	170.6	-110.3
ρ ($\times 10^{-6}$ Ω·m)	1.25	7.81	5.46
κ (W/m·K)	18.7	1.2	1.5

The CMG/BST- and CMG/BT-based ATML slabs with various θ values were prepared by the spark plasma sintering method. The sintered CMG with a diameter of 20 mm was sliced into many disks with a thickness of 1 mm using a diamond wire saw. The CMG disks and BST (BT) po wders were alternately filled into a graphite die and sintered at 450°C with a uniaxial pressure of 30 MPa and soaking time of 60 min under high vacuum. The average thickness of BST (BT) was 0.7 mm, which corresponds to the thickness ratio of CMG $t = d_{CMG}/d_{CMG}+d_{BST(BT)} = 0.59$ with d being the thickness of each layer. The sintered CMG/BST and CMG/BT multilayers were cut into rectangular slabs with a size of $10 \times 8 \times 1$ mm^3 and θ = 0, 15, 30, 45, 60, 75, and 90°.

The two-dimensional temperature distribution and transverse thermoelectric conversion for CMG/BST- and CMG/BT-based ATMLs were measured using an infrared camera and homemade thermoelectric property measurement setup. Figure 1(c) shows a schematic of the measurement configuration, where the ATML sample was bridged between two anodized Al blocks in the *y*-direction with a distance of ~6 mm, one of which acted as a heat source by applying a charge current to connected chip heaters and the other as a heat sink to generate $\nabla_y T$. Here, a region of interest in the ATML sample floated in the air keeping close to the adiabatic condition in *x*-axis, defined as the adiabatic configuration. Meanwhile, by attaching a high thermal conductivity layer to the bottom surface of ATML, the ODTC-induced $\nabla_x T$ can be canceled due to the thermal shunting effect in the parallel thermal circuit [54]. In this work, a 0.5-mm-thick thermally oxidized Si substrate was attached to the ATML sample by a diamond thermal grease, defined as the isothermal configuration. To measure a transverse thermoelectric voltage V_x, two Al-1%Si wires were directly attached on the 10×8 mm^2 top surface with a distance of ~6.5 mm in the *x*-direction by using a wire bonder. To apply a load current I_{load},

*Contact author: ANDO.Fuyuki@nims.go.jp

the 8 × 1 mm^2 side surfaces were covered with a silver paste connected to copper wires. Figure 1(d) shows an infrared image of CMG/BT-based ATML with θ = 45° placed on the sample holder. The central part of 10 × 8 mm^2 surface was covered with an insulating black ink having a high emissivity over 0.94. The observation area for thermography using an infrared camera is defined as a 3.6 × 3.6 mm^2 square centered on the midpoint of the two Al-1%Si electrodes.

III. RESULTS

A. Off-diagonal thermal conduction

We begin with the analytical calculation of the thermal conductivity tensor for CMG/BST- and CMG/BT-based ATMLs following Appendix A and Refs. [51–53]. The measured κ in Table I and t are substituted into Eqs. (A1) and (A2) to calculate κ_{ij}. According to the equations, t and θ are variables for κ_{ij} as well as κ of CMG, BST, and BT. Figures

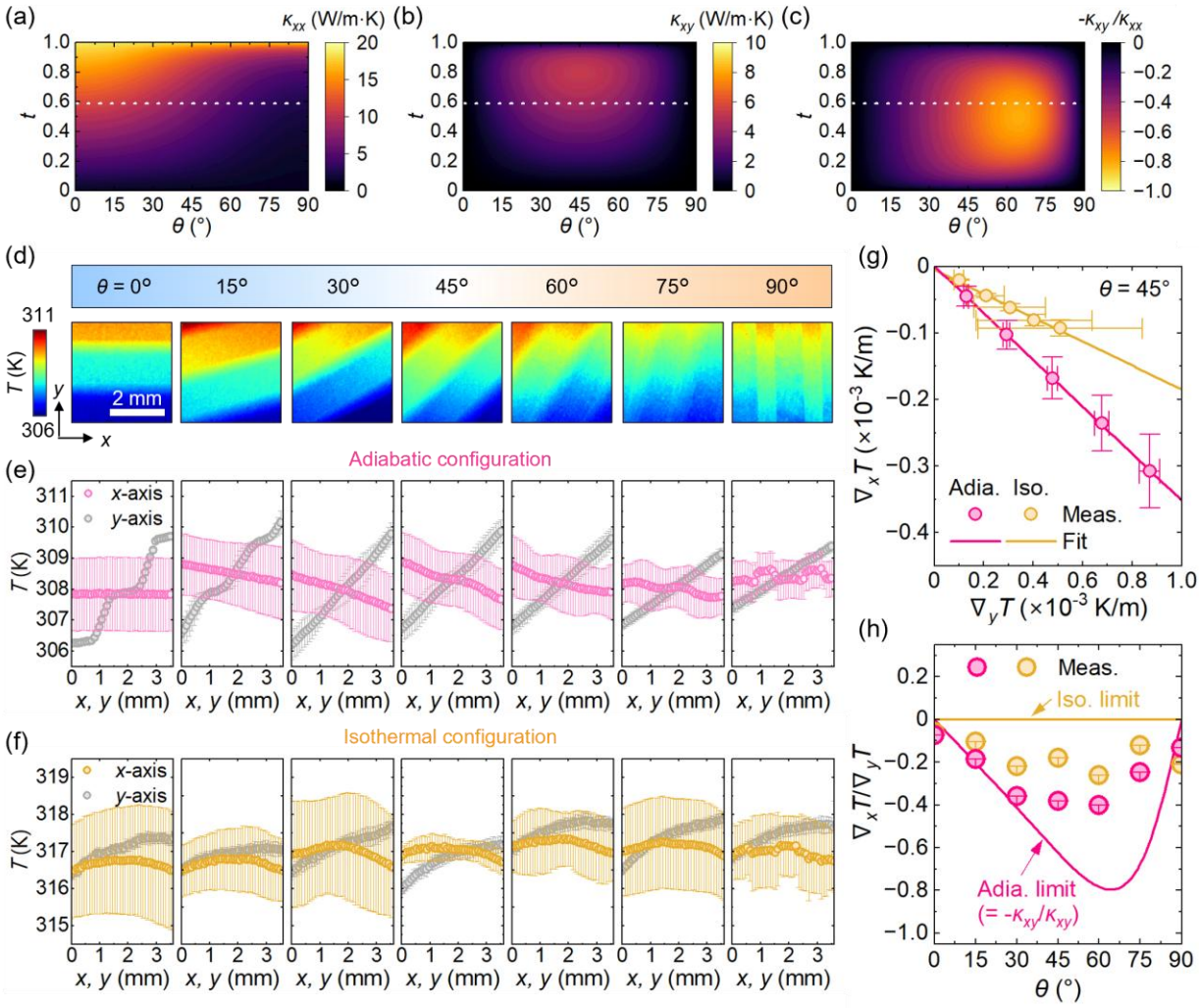

FIG 2. (a)-(c) Contour plots of the calculated (a) κ_{xx}, (b) κ_{xy}, and (c) $-\kappa_{xy}/\kappa_{xx}$. White dotted lines indicate t = 0.59. (d) Thermal images of CMG/BST-based ATMLs at t = 0.59 and various θ values under the application of $\nabla_y T$. (e)-(f) The x- and y-axes line profiles of the average temperature signals in the y- and x-directions for the adiabatic and isothermal configurations. (g) The plot of effective $\nabla_x T$ and $\nabla_y T$ for CMG/BST-based ATML at θ = 45° in the adiabatic and isothermal configurations under various temperature differences between the heat source and sink. (h) The θ dependence of $\nabla_x T/\nabla_y T$ for CMG/BST-based ATMLs in the adiabatic and isothermal configurations with the calculated adiabatic ($-\kappa_{xy}/\kappa_{xx}$ at t = 0.59) and isothermal limits.

*Contact author: ANDO.Fuyuki@nims.go.jp

2(a)–(c) shows the contour plots of κ_{xx}, κ_{xy}, and $-\kappa_{xy}/\kappa_{xx}$ as functions of t and θ for CMG/BST-based ATML. Figure 2(a) shows that κ_{xx} monotonically increases as t (θ) increases (decreases) due to the enhanced contribution of CMG with high κ. Meanwhile, κ_{xy} in Fig. 2(b) shows a different trend maximizing at 45° due to the $\sin\theta\cos\theta$ contribution. As a result, $-\kappa_{xy}/\kappa_{xx}$ in Fig. 2(c) shows a unique θ dependence which minimizes at 64° and relatively moderate t dependence. In the case of CMG/BT-based ATML, $-\kappa_{xy}/\kappa_{xx}$ minimizes at 62°, suggesting that the optimum t and θ to maximize ODTC depend on the balance of κ for constituent materials.

To experimentally confirm the heat current manipulation by ODTC, we observed and analyzed the two-dimensional temperature distribution for our ATMLs in the adiabatic and isothermal configurations. Figure 2(d) shows thermal images in the area indicated by Fig. 1(d) under the application of $\nabla_y T$ for CMG/BST-based ATMLs in the adiabatic configuration. Here, the input heater power was tuned so that the temperature difference between the heat source and sink stabilized at 10.0 ± 0.1 K. All the thermal images represent layered patterns with different angles corresponding to θ, which reflects the difference in κ between CMG and BST. The temperature drastically changes in the BST layers due to the lower κ. To quantitatively discuss ODTC-induced $\nabla_x T$ and $\nabla_y T$ in our ATMLs, we plot the x- and y-axes position dependence of the temperature signals averaged in the y- and x- directions for the adiabatic and isothermal configurations as shown in Fig. 2(e)–(f). The coordinate origin is defined at the lower left corner of the thermal images. In the adiabatic configuration, the negative slope in the x-axis plot is clearly observed only in the middle θ values, whereas those are almost zero at θ = 0° and 90°. This characteristic is consistent with $\kappa_{xy} \propto \sin\theta\cos\theta$ in Fig. 2(b), directly suggesting the appearance of ODTC-induced $\nabla_x T$. The y-axis plot shows the decrease in the positive slope as θ increases, which can result from the increase in κ_{yy} of the ATML samples according to the matrix calculation in Appendix A. Let us see the result in the isothermal configuration in Fig. 2(f). Because of the formation of a parallel thermal circuit with the Si substrate, $\nabla_y T$ is smaller than that in Fig. 2(e) even when the temperature difference between the heat source and sink is the same. Importantly, the negative slope in the x-axis plot is relatively suppressed although not perfectly canceled, suggesting the thermal shunting with the attached Si substrate. The reason for the nonlinear slopes in the x- and y- axis plots in all the θ values is unclear but probably related to the thermal shunting with the side electrodes and heat source/sink through the Si substrate.

We compare the experimentally measured $\nabla_x T/\nabla_y T$ in the adiabatic and isothermal configurations associated with the analytically calculated $-\kappa_{xy}/\kappa_{xx}$ for CMG/BST-based ATMLs. Figure 2(g) shows the plot of effective $\nabla_x T$ and $\nabla_y T$ for CMG/BST-based ATML with θ = 45° in the adiabatic and isothermal configurations under the various temperature differences between the heat source and sink, where the $\nabla_x T$ and $\nabla_y T$ values are determined by the slope of linear fit in Fig. 2(e)–(f). Also, the $\nabla_x T/\nabla_y T$ values are evaluated by the slope of linear fit in Fig. 2(g). The θ dependence of $\nabla_x T/\nabla_y T$ for CMG/BST-based ATMLs as well as the calculated $-\kappa_{xy}/\kappa_{xx}$ at t = 0.59 are depicted in Fig. 2(h). According to Eq. (3), in the ideal adiabatic and isothermal condition, $\nabla_x T/\nabla_y T$ is equal to $-\kappa_{xy}/\kappa_{xx}$ and zero, respectively. The measured $\nabla_x T/\nabla_y T$ in the adiabatic configuration is obviously closer to $-\kappa_{xy}/\kappa_{xx}$ than that in the isothermal configuration, suggesting the induction and suppression of ODTC in the adiabatic and isothermal configurations, respectively. The $\nabla_x T/\nabla_y T$ values quantitatively agree with $-\kappa_{xy}/\kappa_{xx}$ especially at low θ region and reach the minimum value of -0.40 at θ = 60° in the adiabatic configuration owing to the large difference in κ in Table I, which is expected to have a significant impact on transverse thermoelectric performance. The reason for the deviation at higher θ is mentioned in Discussion section. Hereby, we demonstrated the manipulation of the heat current direction and appearance of $\nabla_x T$ through ODTC for ATMLs in the adiabatic condition.

B. Adiabatic transverse thermopower

We phenomenologically formulate the adiabatic transverse thermopower S_{xy}^* by ODSE and the ODTC-induced Seebeck effect for anisotropic materials such as ATMLs. The two-dimensional thermoelectric tensor in the x-y plane for the heat current **q** and electric field **E** is introduced as follows [42–45]:

$$\begin{pmatrix} j_{q,x} \\ j_{q,y} \\ E_x \\ E_y \end{pmatrix} = \begin{pmatrix} S_{xx}T & S_{xy}T & -\kappa_{xx} & -\kappa_{xy} \\ S_{yx}T & S_{yy}T & -\kappa_{yx} & -\kappa_{yy} \\ \rho_{xx} & \rho_{xy} & S_{xx} & S_{xy} \\ \rho_{yx} & \rho_{yy} & S_{yx} & S_{yy} \end{pmatrix} \begin{pmatrix} j_{c,x} \\ j_{c,y} \\ \nabla_x T \\ \nabla_y T \end{pmatrix}. \quad (4)$$

Here, we consider generation of E_x by the application of $\nabla_y T$ under an open-circuit condition in the y-

*Contact author: ANDO.Fuyuki@nims.go.jp

direction ($j_{c,y}$ = 0). Then, the relevant linear-response equations can be written as

$$j_{q,x} = S_{xx}Tj_{c,x} - \kappa_{xx}\nabla_x T - \kappa_{xy}\nabla_y T, \quad (5)$$

$$j_{q,y} = S_{yx}Tj_{c,x} - \kappa_{yx}\nabla_x T - \kappa_{yy}\nabla_y T, \quad (6)$$

$$E_x = \rho_{xx}j_{c,x} + S_{xx}\nabla_x T + S_{xy}\nabla_y T, \quad (7)$$

$$E_y = \rho_{yx}j_{c,x} + S_{yx}\nabla_x T + S_{yy}\nabla_y T. \quad (8)$$

Equations (5)–(8) in the adiabatic condition for the *x*-direction ($j_{q,x}$ = 0) can be solved for $\nabla_y T$ and E_x as

$$\nabla_y T = \frac{S^*_{yx}}{\kappa^*_{yy}}Tj_{c,x} - \frac{1}{\kappa^*_{yy}}j_{q,y}, \quad (9)$$

$$E_x = \rho^*_{xx}j_{c,x} - \frac{S^*_{xy}}{\kappa^*_{yy}}j_{q,y}, \quad (10)$$

where the adiabatic transverse thermopower S^*_{xy} and S^*_{yx} are described by using the isothermal transverse thermopower S_{xy} and S_{yx} as follows:

$$S^*_{xy} = S_{xy} - \frac{\kappa_{xy}}{\kappa_{xx}}S_{xx}, \quad (11)$$

$$S^*_{yx} = S_{yx} - \frac{\kappa_{yx}}{\kappa_{xx}}S_{xx}, \quad (12)$$

where the first term represents the intrinsic ODSE and the second term the ODTC-induced Seebeck effect. In the case of ATMLs, both the Seebeck and thermal conductivity tensors are symmetric (see Appendix A), i.e., $S_{xy} = S_{yx}$, $\kappa_{xy} = \kappa_{yx}$, and hence $S^*_{xy} = S^*_{yx}$. Note that those for the Nernst and thermal Hall effects are antisymmetric due to Onsager's reciprocal relations, i.e., $S_{xy} = -S_{yx}$, $\kappa_{xy} = -\kappa_{yx}$, and hence $S^*_{xy} = -S^*_{yx}$.

Firstly, we calculated and measured S_{xx} to confirm the anisotropic thermoelectric property in ATMLs as the origin of S_{xy}. Fig. 3(a) shows the contour plots of S_{xx} for CMG/BST-based ATML as functions of *t* and θ calculated from Eq. (A11). As *t* decreases (increases) and θ increases (decreases), S_{SE} of BST (CMG) layers dominantly contributes to S_{xx} for CMG/BST-based ATML. Fig. 3(b) shows the θ dependence of S_{xx} at *t* = 0.59, where S_{xx} was measured using the Seebeck-coefficient/electric-resistance measurement system (ZEM-3, ADVANCE RIKO Inc.). The measured S_{xx} value changes depending on θ from negative values for

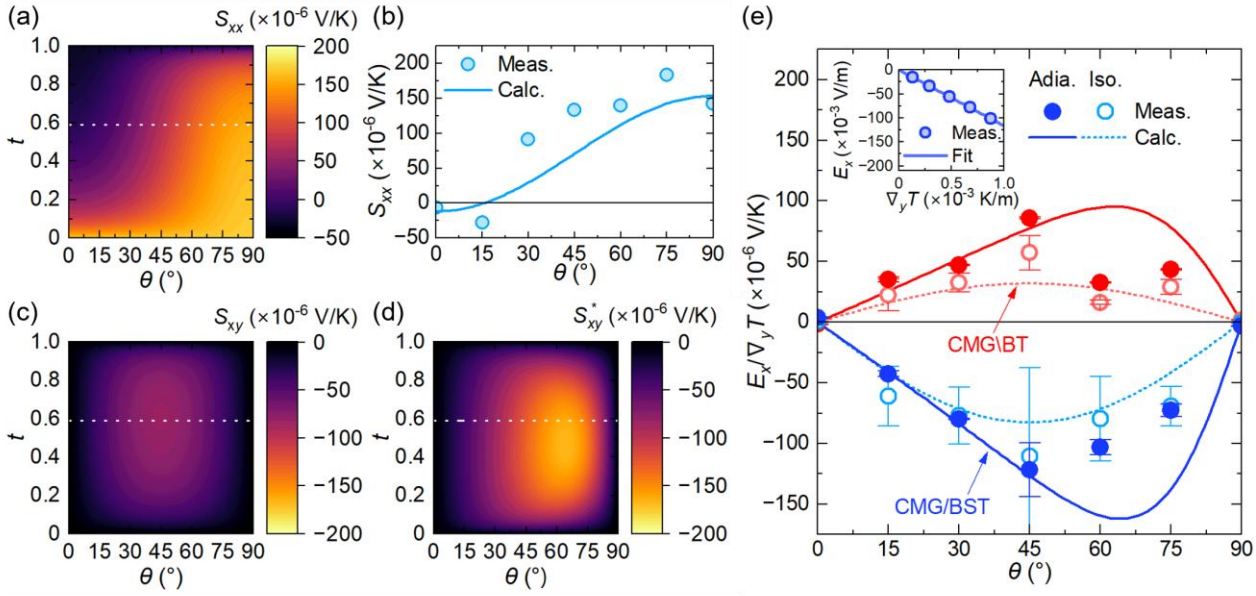

FIG 3. (a) Contour plot of the calculated S_{xx} for CMG/BST-based ATML. (b) The θ dependence of the measured and calculated S_{xx} at *t* = 0.59 with the tiny error bar. (c)-(d) Contour plots of the calculated (c) S_{xy} and (d) S^*_{xy}. (e) The θ dependence of the measured $E_x/\nabla_y T$ in the adiabatic and isothermal configurations and calculated S_{xy} and S^*_{xy} for both CMG/BT- and CMG/BST-based ATMLs. The inset is the $\nabla_y T$ dependence of E_x for CMG/BST-based ATML at θ = 45°.

*Contact author: ANDO.Fuyuki@nims.go.jp

$\theta \leq 15°$ due to the electrical shunting effect in CMG layers to large positive value for $\theta > 15°$, reproducing the analytically calculated values. Thus, we can expect the experimental observation of S_{xy} by ODSE.

Then, we analytically calculate S_{xy} and S^*_{xy}. Figure 3(c) shows the contour plot of S_{xy} as functions of t and θ for CMG/BST-based ATML, calculated based on Eq. (11) and the thermoelectric transport tensors for ATMLs in Appendix A. The S_{xy} value minimizes at 45° in a similar manner to κ_{xy} in Fig. 2(b). On the other hand, because S_{xx} and $-\kappa_{xy}/\kappa_{xx}$ have the different t and θ dependences as shown in Figs. 3(c) and 2(c), S^*_{xy} exhibits a distinct behavior with S_{xy} [Fig. 3(d)]. Owing to the same sign of S_{xy} and $-\kappa_{xy}S_{xx}/\kappa_{xx}$ for $\theta > 15°$, the peak S^*_{xy} is greatly higher than the peak S_{xy} in this study: S^*_{xy} reaches -167.7 μV/K at $t = 0.47$ and $\theta = 64°$, whereas S_{xy} -82.7 μV/K at $t = 0.61$ and $\theta = 45°$. Thus, we naturally expect the improvement of the transverse thermopower through the contribution of ODTC.

Now, we are in the position to experimentally characterize the transverse thermopower $E_x/\nabla_y T$ in the adiabatic and isothermal configurations comparing with S_{xy} and S^*_{xy}. Figure 3(e) shows the measurement results for CMG/BST- and CMG/BT-based ATMLs. The $E_x/\nabla_y T$ values are determined by the slope of linear fit as shown in the inset of Fig. 3(e). Reflecting the opposite sign of S_{SE} for BST and BT, CMG/BST- and CMG/BT-based ATMLs also show the opposite sign of $E_x/\nabla_y T$ (see Eqs. (A6), (A7), and (A10) of Appendix A for details). For CMG/BT-based ATML, S^*_{xy} is larger than S_{xy} in the overall θ region because S_{xx} is negative regardless of θ. Importantly, the experimentally measured $E_x/\nabla_y T$ in the adiabatic configuration is also larger than that in the isothermal configuration regardless of θ, completely matching the analytical calculation. Meanwhile, for CMG/BST-based ATML, S^*_{xy} is larger than S_{xy} for $\theta > 15°$ due to the sign change of S_{xx} [(Fig. 3(b)]. The experimentally measured $E_x/\nabla_y T$ in the adiabatic and isothermal configurations for CMG/BST-based ATML completely reproduces this large and small relationship between S^*_{xy} and S_{xy}, where $E_x/\nabla_y T$ in the adiabatic configuration is larger only for $\theta > 15°$. These results are the direct evidence of the contribution of ODTC to transverse thermoelectric conversion. The $E_x/\nabla_y T$ values quantitatively agree with S^*_{xy} for $\theta \leq 45°$ but get closer to S_{xy} with increasing θ, whose trend is consistent with that of the measured $\nabla_x T/\nabla_y T$ in Fig. 2(h). Although the conventional matrix calculation suggests the optimum S_{xy} of -82.6 μV/K at $\theta = 45°$ for CMG/BST-based ATML, $E_x/\nabla_y T$ measured in the adiabatic condition reaches the much higher value of -121.9 ± 22.2 μV/K, which leads to a significant enhancement of the transverse thermoelectric performance.

C. Transverse thermoelectric performance

We phenomenologically formulate the adiabatic transport properties relevant to $z^*_{xy}T$ for anisotropic materials such as ATMLs. By solving Eqs. (5)–(8), ρ^*_{xx} and κ^*_{yy} defined by Eqs. (9) and (10) can be expressed as

$$\rho^*_{xx} = \rho_{xx} + \left(\frac{S^*_{xy}S^*_{yx}}{\kappa^*_{yy}} + \frac{{S_{xx}}^2}{\kappa_{xx}}\right)T, \qquad (13)$$

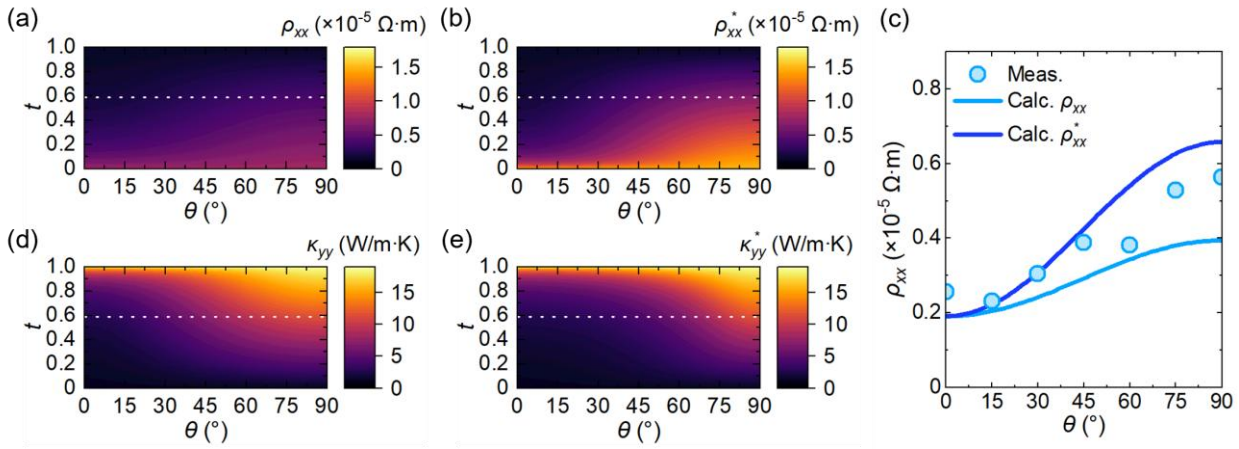

FIG 4. (a)-(b) Contour plots of the calculated (a) ρ_{xx} and (b) ρ^*_{xx} for CMG/BST-based ATML. (c) The θ dependence of the measured and calculated ρ_{xx} at $t = 0.59$ including tiny error bars. (d)-(e) Contour plots of the calculated (d) κ_{yy}, and (e) κ^*_{yy}.

*Contact author: ANDO.Fuyuki@nims.go.jp

$$\kappa_{yy}^{*} = \kappa_{yy} - \frac{\kappa_{xy}\kappa_{yx}}{\kappa_{xx}}. \quad (14)$$

Figures 4(a)–(b) show the analytically calculated ρ_{xx} and ρ_{xx}^{*} as functions of t and θ for CMG/BST-based ATML, indicating the obviously different behaviors between the isothermal and adiabatic conditions as well as S_{xy} and S_{xy}^{*}. As shown in Fig. 4(c), we experimentally measured the θ dependence of ρ_{xx} for CMG/BST-based ATML at t = 0.59 using ZEM-3. ρ_{xx} increases as θ increases in correspondence with the analytical calculation. Because the voltage was measured while applying a pulse current, the measured ρ_{xx} values show a relatively close trend to that in the isothermal condition. As well as ρ_{xx} and ρ_{xx}^{*}, κ_{yy} and κ_{yy}^{*} show the distinct behaviors as functions of t and θ [Figs. 4(d)–(e)]. Due to the symmetric relations of $S_{xy} = S_{yx}$ and $\kappa_{xy} = \kappa_{yx}$, ρ_{xx}^{*} (κ_{yy}^{*}) necessarily exhibits a higher (lower) value than ρ_{xx} (κ_{yy}). As a result, $z_{xy}^{*}T$ is expressed by the replacement of Eq. (1) by Eqs. (10), (12), and (13):

$$z_{xy}^{*}T = \frac{{S_{xy}^{*}}^{2}}{\rho_{xx}^{*}\kappa_{yy}^{*}}T. \quad (15)$$

Note that by substituting the relations of $S_{xy} = -S_{yx}$, $\kappa_{xy} = -\kappa_{yx}$ due to Onsager's reciprocal theory to Eqs. (13)–(14), the adiabatic transport properties for the Nernst effects can be obtained, where κ_{yy}^{*} necessarily exhibits a higher value than κ_{yy} contrary to the case of ATMLs.

Figure 5(a)–(b) shows analytically calculated $z_{xy}T$ and $z_{xy}^{*}T$ values for CMG/BST-based ATML. In general, S_{xy} ($\propto \sin\theta\cos\theta$) maximizes at θ = 45° and both ρ_{xx} and κ_{yy} monotonically decrease as θ decreases [Figs. 3(a), 4(a), and 4(c)]. Thus, the conventional calculation for ATMLs in the isothermal limit necessarily suggests the optimum θ lower than 45° to maximize $z_{xy}T$ [33–35,37]. In fact, Fig. 5(a) shows that $z_{xy}T$ for CMG/BST-based ATML maximizes to be 0.13 at t = 0.56 and θ = 30°. On the other hand, the best θ to maximize S_{xy}^{*} drastically changes from 45° due to the $-\kappa_{xy}S_{xx}/\kappa_{xx}$ term and positions at 64° for CMG/BST-based ATML [Fig 3(c)]. Figure 5(b) shows that, through balancing between high S_{xy}^{*} and low ρ_{xx}^{*} and κ_{yy}^{*}, $z_{xy}^{*}T$ reaches 0.28 at t = 0.44 and θ = 47°, which provides totally different design parameters from the conventional analytical calculation.

Let us compare the transverse thermoelectric performance between the isothermal and adiabatic conditions. Note that the figure of merit cannot be directly used for the fair comparison because the domains of definition are different as follows:

$$0 < z_{xy}T < \infty, \quad (16)$$

$$0 < z_{xy}^{*}T < 1. \quad (17)$$

The presence of ODTC and the Seebeck effect makes it more difficult to get the relation between $z_{xy}T$ and

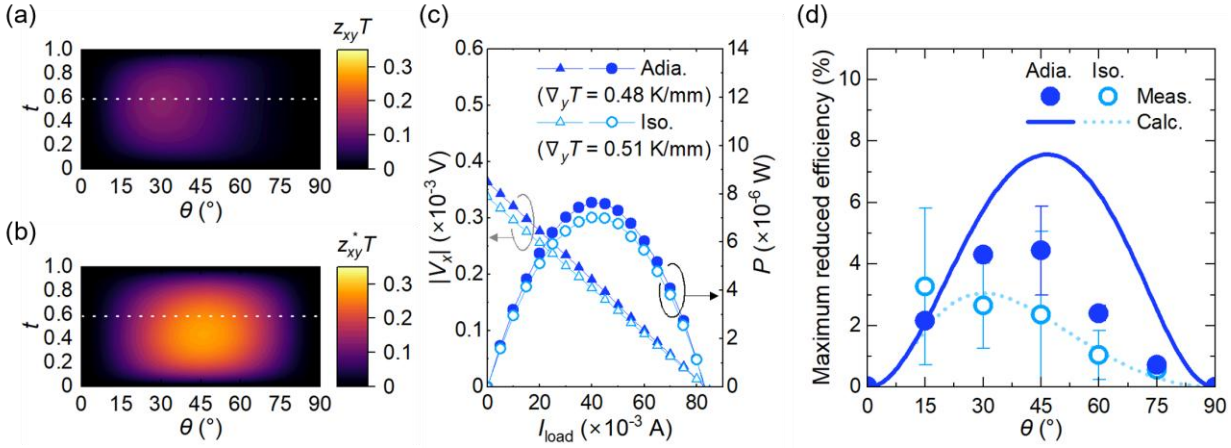

FIG 5. (a)-(b) Contour plots of the calcurated (a) $z_{xy}T$ and (b) $z_{xy}^{*}T$ for CMG/BST-based ATML. (c) The I_{load} dependence of $|V_x|$ and P at $\nabla_y T$ = 0.48 K/mm (0.51) in the adiabatic (isothermal) configuration for CMG/BST-based ATML at t = 0.59 and θ = 45°. (d) The θ dependence of the maximum reduced efficiency in the adiabatic and isothermal configurations together with the calculated η_{xy} and η_{xy}^{*} for CMG/BST-based ATML at t = 0.59.

*Contact author: ANDO.Fuyuki@nims.go.jp

$z^*_{xy}T$ whereas $z^*_{xy}T = z_{xy}T/(1+z_{xy}T)$ was obtained under $S_{xx} = \kappa_{xy} = 0$. Then, we introduce the maximum reduced efficiency for transverse thermoelectric conversion in the isothermal and adiabatic limits (η_{xy} and η^*_{xy}), which enables the fair comparison because the thermoelectric conversion efficiency is expressed by $\eta_{\mathrm{Carnot}}\eta_{xy}$ and $\eta_{\mathrm{Carnot}}\eta^*_{xy}$ with the Carnot efficiency η_{Carnot} for both the isothermal and adiabatic cases:

$$\eta_{xy} = \frac{\sqrt{1+z_{xy}T}-1}{\sqrt{1+z_{xy}T}+1}, \tag{18}$$

$$\eta^*_{xy} = \frac{1-\sqrt{1-z^*_{xy}T}}{1+\sqrt{1-z^*_{xy}T}}. \tag{19}$$

By respectively substituting $z_{xy}T = 0.13$ and $z^*_{xy}T = 0.28$ into Eqs. (18) and (19), η_{xy} = 3.1% in the isothermal limit and η^*_{xy} = 8.1% in the adiabatic limit are obtained. Thus, the change rate in the conversion efficiency is estimated to be 165%, which provides a great impact on the transverse thermoelectric performance.

To experimentally confirm the enhancement of conversion efficiency in the adiabatic condition, we performed the thermoelectric power generation measurements for CMG/BST-based ATML in the adiabatic and isothermal configurations. As shown in Fig. 5(c), the load current I_{load} dependence of $|V_x|$ was measured under the application of $\nabla_y T$ to characterize the output power P (= $I_{\mathrm{load}} \times |V_x|$). Each $|V_x|$ value was obtained after inputting I_{load} and waiting for 10 seconds to stabilize at the thermal equilibrium state. The $|V_x|$ value almost linearly decreases as I_{load} increases due to the internal resistance of CMG/BST-based ATML, resulting in the parabolic-shape P curves. Interestingly, despite the applied $\nabla_y T$ is smaller in the adiabatic configuration in Fig. 5(c), the obtained P is larger owing to the larger open-circuit voltage (V_x at $I_{\mathrm{load}} = 0$) by the constructive contribution from ODTC. Then, we experimentally determine the maximum reduced efficiency as follows:

$$\eta_{xy} = \frac{T_{\mathrm{ave}}}{\Delta_y T}\cdot\frac{P}{A j_{q,y}}. \tag{20}$$

Here, T_{ave} is the average temperature, ΔT_y the temperature difference between the edges attached to the heat source and sink, and A is the cross-sectional area to input $j_{q,y}$ for CMG/BST-based ATMLs, respectively. The $j_{q,y}$ values in the adiabatic and isothermal configurations are estimated from $\kappa^*_{yy}\nabla_y T$ and $\kappa_{yy}\nabla_y T$ as shown in Figs. 4(d)–(e), respectively.

*Contact author: ANDO.Fuyuki@nims.go.jp

Figure 5(d) shows the θ dependence of the measured η_{xy} and η^*_{xy} together with their analytical calculations for CMG/BST-based ATML at t = 0.59. We find that the measured η^*_{xy} is significantly larger than the measured η_{xy} for $\theta > 15°$ as predicted by the analytical calculations. Thus, the difference in η_{xy} and η^*_{xy} is due purely to the contribution from the ODTC-induced Seebeck effect. The measured η^*_{xy} value reaches 4.4% in maximum at θ = 45° whereas η_{xy} remains 2.3%, corresponding to 89% enhancement of the transverse thermoelectric conversion efficiency in the adiabatic configuration. The above calculations and experiments claim that the distinct materials design and performance potential are obtained depending on whether the thermal boundary condition is isothermal or adiabatic.

IV. DISCUSSION

We discuss what factors influence the thermal boundary condition toward the precise estimation of $\nabla_x T/\nabla_y T$ and the resultant transverse thermoelectric performance. Obviously, the heat dissipation at the side surfaces through the convection and radiation enforces the imperfect adiabatic condition even in our measurement setup. Scudder [26] demonstrated that the x : y aspect ratio of the target material also changes the boundary condition through the thermal short-circuit by heat spreaders, i.e., heat source and sink. The shorter length in the y-direction might be one of the reasons why the measured $E_x/\nabla_y T$ for ATMLs in the previous reports were comparable to or less than S_{xy} [33–35,37]. Meanwhile, this work finds that, even if the measurement setup and geometry of the samples were unchanged, the measured $\nabla_x T/\nabla_y T$, $E_x/\nabla_y T$, and η_{xy} gradually deviates from the calculated

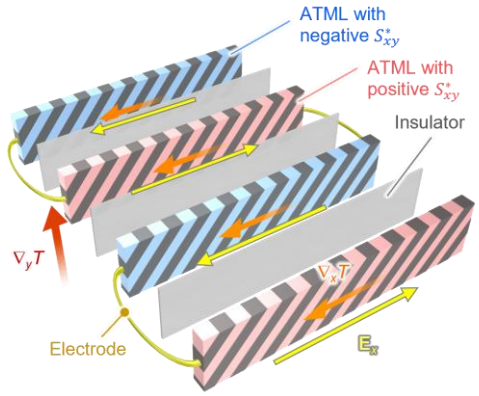

FIG 6. Schematic of a lateral thermopile module utilizing the ODTC-induced transverse thermopower.

$-\kappa_{xy}/\kappa_{xx}$, S^*_{xy}, and η^*_{xy} with increasing θ [Figs. 2(h), 3(e), and 5(d)], meaning that the region of interest changes from the adiabatic to isothermal condition. In light of this observation, the erosion of isothermal boundaries from the heat spreaders ($\nabla_x T = 0$) has a variable influence in this study, i.e., as κ_{yy} increases by increasing θ [Fig. 4(d)], the heat spreaders more and more imposes the isothermal confinement on the positions to measure $\nabla_x T/\nabla_y T$, $E_x/\nabla_y T$, and η_{xy}. In other words, the decrease in κ_{yy} or the optimization of $x : y$ aspect ratio will result in the enhancement of the experimental η_{xy} of 4.4% ideally to η^*_{xy} of 7.6% in the adiabatic limit.

Finally, we present how to utilize the ODTC-induced performance enhancement in transverse thermoelectric devices. Figure 6 shows a schematic of a lateral thermopile structure as an example. The important point is that two kinds of transverse thermoelectric materials with the same sign of $-\kappa_{xy}/\kappa_{xx}$ and the opposite sign of S^*_{xy}, such as our CMG/BT- and CMG/BST-based ATML slabs, are used. By alternately stacking the two materials intermediated by insulator layers and electrically connected side-by-side, a thermally parallel and electrically series circuit is formed. The side surfaces for electrodes need to be thermally isolated from heat spreaders as much as possible. Owing to the unidirectional transverse heat current for each element, the net transverse temperature gradient $\nabla_x T$ will originate without canceling out in the entire module. As a result, the transverse thermopower will be enhanced compared with S_{xy} [Fig. 3(e)] and positively contribute to the output power.

V. CONCLUSIONS

We phenomenologically formulated and experimentally observed an adiabatic transverse thermoelectric performance enhanced by ODTC raising examples of CMG/BT- and CMG/BST-based ATMLs. ODTC induced by an anisotropic thermal conductivity generates a finite transverse temperature gradient and Seebeck-effect-induced thermopower in the adiabatic condition, which is superposed on the isothermal transverse thermopower driven by ODSE. From the two-dimensional temperature distributions on the ATML surfaces in the adiabatic condition, the generation of sizable transverse temperature gradient was observed, which is quantitatively consistent with the calculated ODTC ratio. The resultant adiabatic transverse thermopower in ATMLs was clearly larger than the calculated and measured isothermal ones. By utilizing this ODTC-induced thermopower, we greatly improved the transverse thermoelectric conversion efficiency up to 89% from the conventional isothermal configuration. This work provides a new design for the ODSE materials and devices distinct from the conventional matrix calculations.

*Contact author: ANDO.Fuyuki@nims.go.jp

ACKNOWLEDGMENTS

The authors thank H. Sepehri-Amin and A. Takahagi for valuable discussions and K. Suzuki and M. Isomura for technical supports. This work was supported by ERATO "Magnetic Thermal Management Materials" (No. JPMJER2201) from JST, Grants-in-Aid for Scientific Research KAKENHI (No. 24K17610) from JSPS, and NEC Corporation.

APPENDIX A: CALCURATION OF THERMOELECTRIC TRANSPORT TENSORS FOR ATMLS

First, the thermal conductivity tensor for ATML comprising two materials A and B with different thermal conductivities (κ_{A} and κ_{B}) is introduced following Refs. [51–53]. An A/B-based multilayer exhibits the anisotropic thermal conductivities between the directions parallel and perpendicular to the stacking plane as follows:

$$\kappa_{\parallel} = t\kappa_{\mathrm{A}} + (1-t)\kappa_{\mathrm{B}}, \tag{A1}$$

$$\kappa_{\perp} = \frac{\kappa_{\mathrm{A}} \cdot \kappa_{\mathrm{B}}}{t\kappa_{\mathrm{B}} + (1-t)\kappa_{\mathrm{A}}}. \tag{A2}$$

When we define *x*- or *z*- and *y*-axes as the parallel and perpendicular directions respectively, the thermal conductivity tensor is expressed using Eqs. (A1) and (A2) as

$$\kappa_{ij} = \begin{pmatrix} \kappa_{\parallel} & 0 & 0 \\ 0 & \kappa_{\perp} & 0 \\ 0 & 0 & \kappa_{\parallel} \end{pmatrix}. \tag{A3}$$

The off-diagonal components are zero in the original description. To transform this plain multilayer into ATML, we introduce a rotation around *z*-axis by an angle θ which modifies the original axes to $x' = x\cos\theta + y\sin\theta$ and $y' = -x\sin\theta + y\cos\theta$ by the Jacobian matrix of the coordinate transformation:

$$J = \begin{pmatrix} \cos\theta & \sin\theta & 0 \\ -\sin\theta & \cos\theta & 0 \\ 0 & 0 & 1 \end{pmatrix}. \tag{A4}$$

The thermal conductivity tensor is modified through this rotation for the ATML structure, resulting in the finite off-diagonal components as

$$\kappa_{ij} = \frac{J\kappa_{i'j'}J^T}{\det(J)} = \begin{pmatrix} \kappa_\parallel \cos^2\theta + \kappa_\perp \sin^2\theta & (\kappa_\parallel - \kappa_\perp)\sin\theta\cos\theta & 0 \\ (\kappa_\parallel - \kappa_\perp)\sin\theta\cos\theta & \kappa_\parallel \sin^2\theta + \kappa_\perp \cos^2\theta & 0 \\ 0 & 0 & \kappa_\parallel \end{pmatrix}, \quad \text{(A5)}$$

where $\boldsymbol{J}^{\mathbf{T}}$ denotes the transpose of $\boldsymbol{J}$, and det($\boldsymbol{J}$) the determinant.

The Seebeck and electrical resistivity tensors (S_{ij} and ρ_{ij}) are formulated for A/B-based ATML based on the Goldsmid's method [32]. The Seebeck coefficients and electrical resistivities in the directions parallel and perpendicular to the stacking plane are analytically calculated using thermoelectric transport parameters ($S_{\mathrm{SE,A}}$, $S_{\mathrm{SE,B}}$, ρ_{A} and ρ_{B}) as follows:

$$S_{\mathrm{SE},\parallel} = \frac{t\rho_{\mathrm{B}}S_{\mathrm{SE,A}} + (1-t)\rho_{\mathrm{A}}S_{\mathrm{SE,B}}}{t\rho_{\mathrm{B}} + (1-t)\rho_{\mathrm{A}}}, \quad \text{(A6)}$$

$$S_{\mathrm{SE},\perp} = \frac{t\kappa_{\mathrm{B}}S_{\mathrm{SE,A}} + (1-t)\kappa_{\mathrm{A}}S_{\mathrm{SE,B}}}{t\kappa_{\mathrm{B}} + (1-t)\kappa_{\mathrm{A}}}, \quad \text{(A7)}$$

$$\rho_\parallel = \frac{\rho_{\mathrm{A}} \cdot \rho_{\mathrm{B}}}{t\rho_{\mathrm{B}} + (1-t)\rho_{\mathrm{A}}}, \quad \text{(A8)}$$

$$\rho_\perp = t\rho_{\mathrm{A}} + (1-t)\rho_{\mathrm{B}}. \quad \text{(A9)}$$

Following the completely same coordinate transformation by a rotation matrix as Eqs. (A3)−(A5), S_{ij} and ρ_{ij} are obtained. The components relevant to this work are shown as

$$S_{xy} = \left(S_{\mathrm{SE},\parallel} - S_{\mathrm{SE},\perp}\right)\sin\theta\cos\theta, \quad \text{(A10)}$$

$$S_{xx} = S_{\mathrm{SE},\parallel}\cos^2\theta + S_{\mathrm{SE},\perp}\sin^2\theta, \quad \text{(A11)}$$

$$\rho_{xx} = \rho_\parallel \cos^2\theta + \rho_\perp \sin^2\theta. \quad \text{(A12)}$$

[1] A. Von Ettingshausen and W. Nernst, Ueber das Auftreten electromotorischer Kräfte in Metallplatten, welche von einem Wärmestrome durchflossen werden und sich im magnetischen Felde befinden, Ann. Phys. **265**, 343 (1886).

[2] M. H. Norwood, Theory of Nernst Generators and Refrigerators, J. Appl. Phys. **34**, 594 (1963).

[3] Y. Sakuraba, Potential of thermoelectric power generation using anomalous Nernst effect in magnetic materials, Scr. Mater. **111**, 29 (2016).

[4] K. Uchida and J. P. Heremans, Thermoelectrics: From longitudinal to transverse, Joule **6**, 2240 (2022).

[5] G. E. W. Bauer, E. Saitoh, and B. J. Van Wees, Spin caloritronics, Nat. Mater. **11**, 391 (2012).

[6] S. R. Boona, R. C. Myers, and J. P. Heremans, Spin caloritronics, Energy Environ. Sci. **7**, 885 (2014).

[7] K. Uchida, Transport phenomena in spin caloritronics, Proc. Jpn. Acad. Ser. B **97**, 69 (2021).

[8] B. Yan and C. Felser, Topological Materials: Weyl Semimetals, Annu. Rev. Condens. Matter Phys. **8**, 337 (2017).

[9] C. Fu, Y. Sun, and C. Felser, Topological thermoelectrics, APL Mater. **8**, 040913 (2020).

[10] B. A. Bernevig, C. Felser, and H. Beidenkopf, Progress and prospects in magnetic topological materials, Nature **603**, 41 (2022).

[11] T. C. Harman, J. M. Honig, S. Fischler, and A. E. Paladino, The Nernst-Ettingshausen energy conversion figure of merit for Bi and Bi-4% Sb alloys, Solid State Electron. **7**, 505 (1964).

[12] W. M. Yim and A. Amith, Bi-Sb alloys for magneto-thermoelectric and thermomagnetic cooling, Solid State Electron. **15**, 1141 (1972).

[13] M. Ikhlas, T. Tomita, T. Koretsune, M. T. Suzuki, D. Nishio-Hamane, R. Arita, Y. Otani, and S. Nakatsuji, Large anomalous Nernst effect at room temperature in a chiral antiferromagnet, Nat. Phys. **13**, 1085 (2017).

[14] A. Sakai Y. P. Mizuta, A. A. Nugroho, R. Sihombing, T. Koretsune, M. Suzuki, N. Takemori, R. Ishii, D. Nishio-Hamane, R. Arita et al., Giant anomalous Nernst effect and quantum-critical scaling in a ferromagnetic semimetal, Nat. Phys. **14**, 1119 (2018).

[15] H. Reichlova, R. Schlitz, S. Beckert, P. Swekis, A. Markou, Y. Chen, D. Kriegner, S. Fabretti, G. H. Park, A. Niemann et al., Large

*Contact author: ANDO.Fuyuki@nims.go.jp

anomalous Nernst effect in thin films of the Weyl semimetal Co_2MnGa, Appl. Phys. Lett. **113**, 212405 (2018).

[16] A. Miura, H. Sepehri-Amin, K. Masuda, H. Tsuchiura, Y. Miura, R. Iguchi, Y. Sakuraba, J. Shiomi, K. Hono, and K. Uchida, Observation of anomalous Ettingshausen effect and large transverse thermoelectric conductivity in permanent magnets, Appl. Phys. Lett. **115**, 222403 (2019).

[17] A. Sakai, S. Minami, T. Koretsune, T. Chen, T. Higo, Y. Wang, T. Nomoto, M. Hirayama, S. Miwa, D. Nishio-Hamane, F. Ishii et al., Iron-based binary ferromagnets for transverse thermoelectric conversion, Nature **581**, 53 (2020).

[18] Y. Pan, C. Le, B. He, S. J. Watzman, M. Yao, J. Gooth, J. P. Heremans, Y. Sun, and C. Felser, Giant anomalous Nernst signal in the antiferromagnet $YbMnBi_2$, Nat. Mater. **21**, 203 (2022).

[19] P. Li, P. Qiu, Q. Xu, J. Luo, Y. Xiong, J. Xiao, N. Aryal, Q. Li, L. Chen, and X. Shi, Colossal Nernst power factor in topological semimetal $NbSb_2$, Nat. Commun. **13**, 7612 (2022).

[20] F. Ando, T. Hirai, and K. Uchida, Permanent-magnet-based transverse thermoelectric generator with high fill factor driven by anomalous Nernst effect, APL Energy **2**, 016103 (2024).

[21] T. C. Chuang, P. L. Su, P. H. Wu, and S. Y. Huang, Enhancement of the anomalous Nernst effect in ferromagnetic thin films, Phys. Rev. B **96**, 174406 (2017).

[22] B. He, C. Şahin, S. R. Boona, B. C. Sales, Y. Pan, C. Felser, M. E. Flatté, and J. P. Heremans, Large magnon-induced anomalous Nernst conductivity in single-crystal MnBi, Joule **5**, 3057 (2021).

[23] R. Gautam, T. Hirai, A. Alasli, H. Nagano, T. Ohkubo, K. Uchida, and H. Sepehri-Amin, Creation of flexible spin-caloritronic material with giant transverse thermoelectric conversion by nanostructure engineering, Nat. Commun. **15**, 2184 (2024).

[24] B. He, Y. Wang, M. Q. Arguilla, N. D. Cultrara, M. R. Scudder, J. E. Goldberger, W. Windl, and J. P. Heremans, The Fermi surface geometrical origin of axis-dependent conduction polarity in layered materials, Nat. Mater. **18**, 568 (2019).

[25] M. R. Scudder, B. He, Y. Wang, A. Rai, D. G. Cahill, W. Windl, J. P. Heremans, and J. E. Goldberger, Highly efficient transverse thermoelectric devices with Re_4Si_7 crystals, Energy Environ. Sci. **14**, 4009 (2021).

[26] M. R. Scudder, K. G. Koster, J. P. Heremans, and J. E. Goldberger, Adiabatic and isothermal configurations for Re_4Si_7 transverse thermoelectric power generators, Appl. Phys. Rev. **9**, 021420 (2022).

[27] Y. Goto, H. Usui, M. Murata, J. E. Goldberger, J. P. Heremans, and C. H. Lee, Band Anisotropy Generates Axis-Dependent Conduction Polarity of Mg_3Sb_2 and Mg_3Bi_2, Chem. Mater. **36**, 2018 (2024).

[28] H. Manako, S. Ohsumi, Y. J. Sato, R. Okazaki, and D. Aoki, Large transverse thermoelectric effect induced by the mixed-dimensionality of Fermi surfaces, Nat. Commun. **15**, 3907 (2024).

[29] C. Zhou, S. Birner, Y. Tang, K. Heinselman, and M. Grayson, Driving Perpendicular Heat Flow: (p×n)-Type Transverse Thermoelectrics for Microscale and Cryogenic Peltier Cooling, Phys. Rev. Lett. **110**, 227701 (2013).

[30] Y. Tang, B. Cui, C. Zhou, and M. Grayson, $p \times n$-Type Transverse Thermoelectrics: A Novel Type of Thermal Management Material, J. Electron. Mater. **44**, 2095 (2015).

[31] C. Reitmaier, F. Walther, and H. Lengfellner, Transverse thermoelectric devices, Appl. Phys. A Mater. Sci. Process. **99**, 717 (2010).

[32] H. J. Goldsmid, Application of the transverse thermoelectric effects, J. Electron. Mater. **40**, 1254 (2011).

[33] T. Kanno, K. Takahashi, A. Sakai, H. Tamaki, H. Kusada, and Y. Yamada, Detection of thermal radiation, sensing of heat flux, and recovery of waste heat by the transverse thermoelectric effect, J. Electron. Mater. **43**, 2072 (2014).

[34] X. Mu, H. Zhou, W. Zhao, D. He, W. Zhu, X. Nie, Z. Sun, and Q. Zhang, High-performance $YbAl_3/Bi_{0.5}Sb_{1.5}Te_3$ artificially tilted multilayer thermoelectric devices via material genome engineering method, J. Power Sources **430**, 193 (2019).

[35] F. Ando, T. Hirai, A. Alasli, H. Sepehri-Amin, Y. Iwasaki, H. Nagano, and K. I. Uchida, Multifunctional composite magnet realizing record-high transverse thermoelectric generation, Energy Environ. Sci. **18**, 4068 (2025).

[36] K. Uchida, T. Hirai, F. Ando, and H. Sepehri-Amin, Hybrid Transverse Magneto-Thermoelectric Cooling in Artificially Tilted

*Contact author: ANDO.Fuyuki@nims.go.jp

Multilayers, Adv. Energy Mater. **14**, 2302375 (2024).
[37] T. Hirai, F. Ando, H. Sepehri-Amin, and K. Uchida, Hybridizing anomalous Nernst effect in artificially tilted multilayer based on magnetic topological material, Nat. Commun. **15**, 9643 (2024).
[38] H. B. Callen, A Note on the Adiabatic Thermoelectric Effects, Phys. Rev. **85**, 16 (1952).
[39] A. F. Ioffe, *Semiconductor Thermoelements and Thermoelectric Cooling* (Infosearch, London, 1957).
[40] D. A. Wright, Theory of the Nernst-Ettingshausen generator, Brit. J. Appl. Phys. **13**, 583 (1962).
[41] K. Uchida, H. Adachi, T. Kikkawa, A. Kirihara, M. Ishida, S. Yorozu, S. Maekawa, and E. Saitoh, Thermoelectric Generation Based on Spin Seebeck Effects, Proc. IEEE **104**, 1946 (2016).
[42] R. T. Delves, Figure of merit for Ettingshausen cooling, Brit. J. Appl. Phys. **15**, 105 (1964).
[43] R. T. Delves, Thermomagnetic effects in semiconductors and semimetals, Rep. Prog. Phys. **28**, 249 (1965).
[44] C. F. Kooi, R. B. Horst, K. F. Cuff, and S. R. Hawkins, Theory of the Longitudinally Isothermal Ettingshausen Cooler, J. Appl. Phys. **34**, 1735 (1963).
[45] R. B. Horst, Thermomagnetic figure of merit: Bismuth, J. Appl. Phys. **34**, 3246 (1963).
[46] L. De'Medici, Thermomagnetic Mechanism for Self-Cooling Cables, Phys. Rev. Appl. **5**, 024001 (2016).
[47] M. M. H. Polash and D. Vashaee, Infinite-stage Nernst-Ettingshausen Cryocooler for Practical Applications, Phys. Rev. Appl. **15**, 014011 (2021).
[48] G. Park, S. Kang, H. Lee, and W. Choi, Tunable multifunctional thermal metamaterials: Manipulation of local heat flux via assembly of unit-cell thermal shifters, Sci. Rep. **7**, 41000 (2017).
[49] I. Peralta, V. D. Fachinotti, and J. C. Álvarez Hostos, A Brief Review on Thermal Metamaterials for Cloaking and Heat Flux Manipulation, Adv. Eng. Mater. **22**, 1901034 (2020).
[50] J. Wang, G. Dai, and J. Huang, Thermal Metamaterial: Fundamental, Application, and Outlook, iScience **23**, 101637 (2020).
[51] K. P. Vemuri and P. R. Bandaru, Geometrical considerations in the control and manipulation of conductive heat flux in multilayered thermal metamaterials, Appl. Phys. Lett. **103**, 133111 (2013).
[52] K. P. Vemuri, F. M. Canbazoglu, and P. R. Bandaru, Guiding conductive heat flux through thermal metamaterials, Appl. Phys. Lett. **105**, 193904 (2014).
[53] P. R. Bandaru, K. P. Vemuri, F. M. Canbazoglu, and R. S. Kapadia, Layered thermal metamaterials for the directing and harvesting of conductive heat, AIP Adv. **5**, 053403 (2015).
[54] S. J. Watzman, T. M. McCormick, C. Shekhar, S. C. Wu, Y. Sun, A. Prakash, C. Felser, N. Trivedi, and J. P. Heremans, Dirac dispersion generates unusually large Nernst effect in Weyl semimetals, Phys. Rev. B **97**, 161404(R) (2018).

*Contact author: ANDO.Fuyuki@nims.go.jp